ELSEVIER

Surface Science 489 (2001) 107–125

SURFACE SCIENCE

www.elsevier.com/locate/susc

Properties of oxygen sites at the $MoO_3(0\,1\,0)$ surface: density functional theory cluster studies and photoemission experiments

R. Tokarz-Sobieraj [a], K. Hermann [b,*], M. Witko [a], A. Blume [c], G. Mestl [c], R. Schlögl [c]

[a] *Institute of Catalysis and Surface Chemistry, Polish Academy of Sciences, ul. Niezapominajek, 30239 Cracow, Poland*
[b] *Department of Theory, Fritz-Haber-Institut der Max-Planck-Gesellschaft, Faradayweg 4-6, D-14195 Berlin, Germany*
[c] *Department of Inorganic Chemistry, Fritz-Haber-Institut der Max-Planck-Gesellschaft, Faradayweg 4-6, D-14195 Berlin, Germany*

Received 13 December 2000; accepted for publication 4 May 2001

Abstract

Ab initio density functional theory cluster studies on the $MoO_3(0\,1\,0)$ surface as well as ultraviolet photoemission (UPS) experiments on well-crystallized single phase Mo oxides are carried out to examine the electronic structure of the oxide systems. In addition, electronic details of different surface oxygen vacancies are studied by appropriate vacancy clusters. Calculations on embedded clusters as large as $Mo_{15}O_{56}H_{22}$ confirm the mixed covalent/ionic character of the oxide. The computed width of the O 2sp dominated valence band region of MoO_3, about 7 eV, agrees well with the present photoemission data for $MoO_3(0\,1\,0)$ samples. The overall shape of the computed densities of states (DOS) in the O 2sp region of MoO_3 is rather similar to the measured UPS intensity curves indicating weak energy dependence of corresponding transition matrix elements. Calculated vacancy energies for the different surface oxygen sites at $MoO_3(0\,1\,0)$ yield rather large values, 6.8–7.6 eV, which shows that oxygen is bound quite strongly to the substrate. Vacancy formation leads to reduction of neighboring molybdenum centers which expresses itself by increased metal d electron occupation and corresponding DOS contributions above the O 2sp region. This is consistent with the experimental UPS data for $MoO_3(0\,1\,0)$ where oxygen vacancies have been introduced by mild ion bombardment. It is further supported by the present UPS data for well-crystallized intermediate molybdenum oxides, such as $Mo_{18}O_{52}$, Mo_8O_{23}, or Mo_4O_{11}. These oxides show, depending on the degree of reduction, one or two additional peaks above the valence band. Characteristic changes in the intensity ratios of the O 2sp peaks can be interpreted on the basis of the theoretical DOS results as a preferential loss of bridging oxygen from the MoO_3 lattice. Mild ion bombardment, a technique which is often used to clean surfaces in UHV experiments, results in the case of $MoO_3(0\,1\,0)$ in considerable surface reduction. The reduced Mo species is comparable to that in MoO_2 as indicated by the UP spectra. Therefore, mild ion bombardment cannot be considered a suitable tool for the preparation of molybdenum oxide surfaces.

Keywords: Molybdenum oxides; Oxygen; Photoemission (total yield); Density functional calculations; Clusters

* Corresponding author. Tel.: +49-30-84134812; fax: +49-30-84134701.
E-mail address: hermann@fhi-berlin.mpg.de (K. Hermann).

0039-6028/01/$ - see front matter
PII: S0039-6028(01)01169-4

1. Introduction

Molybdenum oxides in combination with other elements, such as bismuth, vanadium, cobalt, or aluminum, are used as highly active and selective catalysts for many reactions of very different type. Examples of commercial processes are isomerization, polymerization, and production of formaldehyde and acronitrile [1–3]. Due to the high industrial relevance of Mo-based catalysts it is important to improve their reaction performance, for example, by considering ternary or quaternery mixed oxides with V, W, Nb, Ta [4–11] or by adding Cu or Sb as promoters [12–20]. In addition, fundamental understanding of microscopic details of the catalysts has to be gained as a pre-requisite for future material science leading to tailor-made selective catalysts.

Catalytic properties of mixed molybdenum oxides can be discussed in terms of compound and surface structure sensitivity where both concepts are interrelated and result from local geometry and electronic properties of the active sites. Compound sensitivity is clearly seen in all phases of molybdenum oxides of intermediate composition, produced by successive reduction of MoO_3, as a result of the different degree of Mo reduction. Other examples are ordered oxides, where Mo ions are stabilized in different oxidation states. They can form series of oxygen deficient materials known as Magneli phases [21–31], where defects (oxygen vacancies) order and result in extended shear structures. Most of these phases are catalytically active for partial oxidation [32]. Compound sensitivity, which results from chemical composition and special crystal geometry, may be responsible for the fact that only one out of many possible Mo oxide phases exhibits highest selectivity and activity.

It is well known that molybdenum oxides can exhibit pronounced crystallographic anisotropy. As a result, different exposed crystal faces have different catalytic behavior, and, therefore, participate in various elementary steps of catalytic reactions [33,34]. This phenomenon, known as surface sensitivity, originates from the local environment of active sites and the orientation of the surface where the active sites are located. For example, oxygen basicity is found to increase with decreasing Mo–O bond strength occurring at different surfaces and may lead to different catalytic behavior. The importance of this factor for hydrocarbon oxidation reactions has become a subject of lively discussion in recent years [1–3,11,33–47]. Here one can mention the selective conversion of propylene to acrolein [35–41] at molybdenum trioxide surfaces. The two conversion steps, hydrogen abstraction from and oxygen insertion into the hydrocarbon, are found to take place at different crystal faces of MoO_3 [10]. Hydrogen abstraction occurs at the (0 0 1) or (1 0 0) crystal faces, whereas nucleophilic addition of oxygen into the allylic species takes place at the basal (0 1 0) face [39,40]. The dependence of catalytic properties on the ratio of exposed (1 0 0) and (0 1 0) faces in MoO_3 catalysts was also reported by Volta [41]. Mo=O double bonds were proposed to be active for formaldehyde formation [48–51], while bridging Mo–O–Mo sites were responsible for the transformation into dimethyl ether [51]. In all oxidation processes discussed above, MoO_3 surface oxygen participates and leads to the oxygenated species.

All oxide phases may also expose different types of oxygen vacancies at their surfaces. These vacancies may undergo re-oxidation by gaseous oxygen or may give rise to extended (rather than point) defects [21,54]. In the latter process, known also as crystallographic shear, changes in the metal-to-oxygen ratio (stoichiometry) are accompanied by rearrangements of the elementary metal–oxygen polyhedral units. Haber [10] proposed that the formation of crystallographic shear planes might be one of the factors creating the ability of these structures to insert oxygen into the organic species in the selective oxidation process. The shear mechanism is supported by quantum chemical calculations on the interaction of MoO_6 octahedra in a Mo_2O_{10} cluster [52] where the edge-linked geometry without a vacancy is energetically more favorable than the corner-linked geometry (with a vacancy). However, the formation of crystallographic shear planes cannot exclude the existence of point defects at MoO_3 surfaces [53,55].

For partial oxidation reactions, compound and surface structure sensitivity has been discussed in

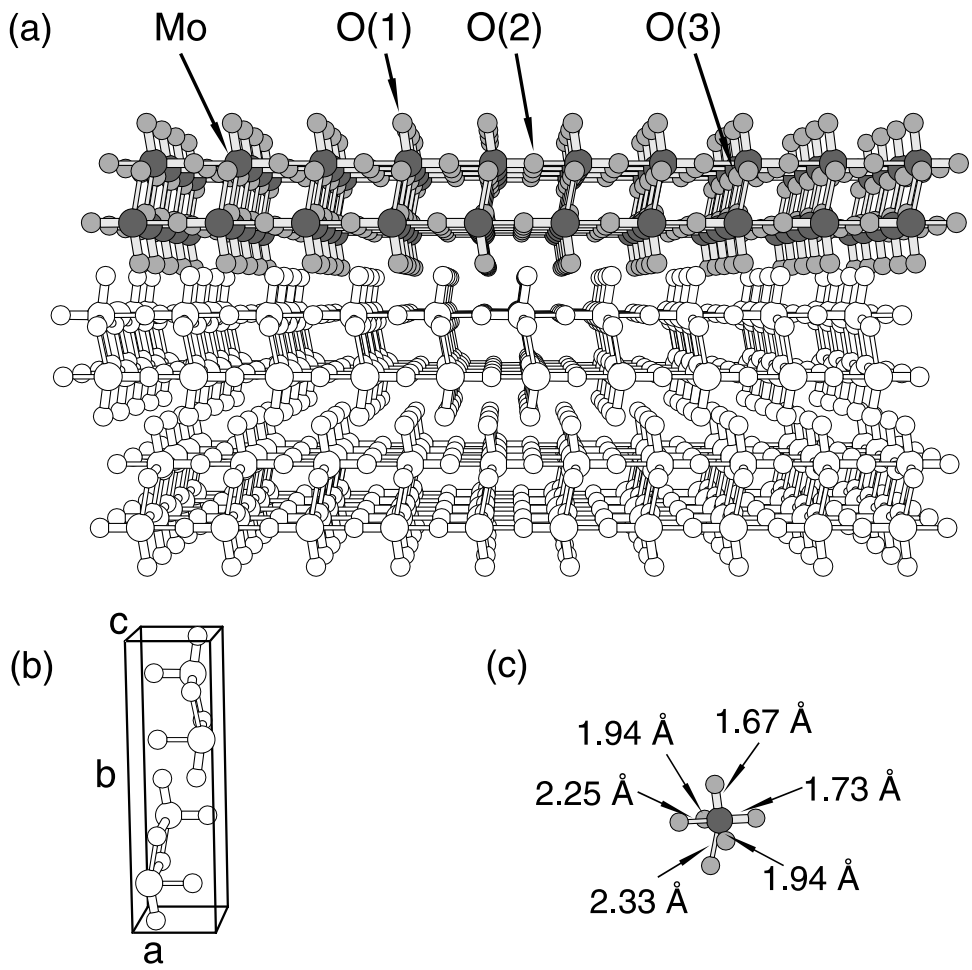

Fig. 1. (a) Crystal structure of orthorhombic MoO_3 with netplane stacking along the (0 1 0) direction. Molybdenum (oxygen) centers are shown by large (small) balls where those of the topmost bi-layer are shaded in dark/light gray. Non-equivalent oxygen centers, O(1–3), and molybdenum centers are labeled accordingly. (b) Elementary unit cell of bulk MoO_3 containing four MoO_3 units. (c) Octahedral MoO_6 building unit with values of interatomic Mo–O distances added.

many studies [1–3,10,15,33–47,57–60]. The strong anisotropy of Mo–O bonding (see also Fig. 1c) implies the validity of surface structure sensitivity. In many studies it was neglected that surface imperfections and/or the notorious instability of highly oxidized surfaces, even of model MoO_3 samples, lead always to a substantial amount of defects which represent all Mo-bond situations. Thus the controversy about the structure sensitivity may be traced back to a lack of structural definition of samples rather than to a basic problem. In this situation a rigorous study of the surface catalytic properties of MoO_3 would be a cornerstone in any attempt to disentangle the complex functions of technical catalysts. This was attempted before in several surface science-inspired studies [61–63]. In these studies the notorious instability of the samples and special treatment conditions for maintaining a usually defective and thus conducting surface were extensively discussed. Electronic properties of surfaces were investigated and valence band spectra were

tentatively assigned to local structural features of the MoO_3 motif. The relation of these studies to practical catalysis is, however, uncertain.

The degree of reduction or the defect density of the model systems cannot be related to that of practical catalysis because of structural and functional deficits of the model system. Pure binary MoO_3 is for most relevant reactants (except of highly activated alcohol molecules) either catalytically inactive or requires extremely high temperatures such that the structure is not stable and is reduced to metallic oxides (transient total oxidation 'activity'), which are also inactive in catalytic conversions. Thus the promoters mentioned above are essential for the function of the selective oxidation systems but are not incorporated into the binary model system. In addition, the structures of real operating catalyst systems are either not known in detail or highly complex [29–31]. Thus, a direct correlation between the real catalyst and corresponding model systems cannot be made. The present work builds upon the previous studies but utilizes a series of samples prepared by chemical vapor phase transport (CVT), a method which allows to synthesize single phase binary oxide systems in qualities suitable for surface science studies. In this work the spectroscopic results of the new model system are related to literature data and compared with rigorous theoretical analysis comprising the stoichiometric system and the process of defect formation. In future work these studies will be extended to the analysis of ternary oxide systems accessible in the same quality as the binary oxides described here.

In the theoretical part of this work, we study the local electronic structure of the $MoO_3(0\,1\,0)$ surface using density functional theory (DFT) cluster models. Embedded surface clusters, as large as $Mo_{15}O_{56}H_{22}$, represent sections of the elementary bi-layer at the substrate surface. In addition, surface oxygen vacancies are considered by appropriate $Mo_{15}O_{56}H_{22}$–O clusters and their influence on the geometric, electronic, and energetic behavior at the $MoO_3(0\,1\,0)$ surface is examined. The electronic structure of the surface systems, characterized by corresponding total and partial valence densities of states (DOS), are compared with the present experimental photoemission data.

In the experimental part of this work, ultraviolet photoemission (UPS) measurements are carried out to study the valence band region of single crystal MoO_3 and of well-crystallized (single-phase) intermediate oxides between MoO_3 and MoO_2, such as Mo_4O_{11}, Mo_8O_{23}, and $Mo_{18}O_{52}$. Further, oxygen vacancies are introduced at the MoO_3 surface by mild ion bombardment, which is often used in UHV experiments for surface cleaning. For both the MoO_3 with oxygen vacancies and the set of intermediate oxides, the intensity ratio of the O 2sp peaks in the valence band region changes and additional intensity is observed in the band gap. The former result can be interpreted by the cluster calculations as due to preferential loss of bridging oxygen upon reduction while the latter is found to be due to Mo 4d contributions originating from reduction of Mo ions near the vacancies. Thus, the UPS results suggest that even mild ion bombardment can reduce the MoO_3 surface substantially leading to photoemission comparable to that of MoO_2 surfaces.

2. Technical details

2.1. Theoretical

Bulk MoO_3 forms an orthorhombic crystal, cp. Fig. 1a, with lattice constants $a = 3.963$ Å, $b = 13.855$ Å, $c = 3.696$ Å [56], and an elementary cell containing four elemental units, see. Fig. 1b. The bulk crystal consists of bi-layer sheets parallel to the (0 1 0) netplane (see Fig. 1a where one bi-layer is labeled by shaded atom balls). Each bi-layer can be described by planes of corner-linked octahedra. The octahedral MoO_6 building unit in bulk MoO_3 is severely distorted, as shown in Fig. 1c, and contains metal oxygen bonds whose lengths vary between 1.68 and 2.33 Å, see Fig. 1c. The largest values refer to oxygen centers which are shared by neighboring octahedra of the two sublayers within the bi-layer while the smallest bond lengths are those for oxygen at the top and bottom of the bi-layer. Adjacent bi-layers interact only weakly with each other which explains why the (0 1 0) direction parallel to the bi-layers defines cleavage planes of the MoO_3 crystal. The weak

electronic coupling between adjacent (0 1 0) bi-layers in MoO_3, which has been verified by experiment [1] and theory [64,65], justifies the use of single bi-layers as appropriate models of the MoO_3(0 1 0) surface. This surface contains three types of structurally different surface oxygen centers, see Fig. 1a. First, the terminal (molybdenyl) oxygen, O(1), is coordinated to one molybdenum atom directly below at a distance of 1.67 Å. Second, the asymmetric bridging oxygen, O(2), is located asymmetrically between two Mo centers at the surface layer at distances 1.73 and 2.25 Å, respectively. Third, the symmetric bridging oxygen, O(3), is placed symmetrically between two Mo centers of the surface layer with distances 1.94 Å each, and is linked to another Mo center of the underlying sublayer with a distance of 2.33 Å.

The bi-layers of MoO_3 can be described alternatively by chains of corner-sharing MoO_4 tetrahedra along the (0 0 1) direction [56]. The distorted MoO_4 tetrahedra are defined by four O centers surrounding Mo at distances of 1.68, 1.73 and 2×1.94 Å. Parallel arrangements of tetrahedra chains along the (0 1 0) netplanes represent one half of the MoO_3 bi-layers. Adjacent bi-layers are connected by weak interaction which explains the easy cleavage of MoO_3 crystals along the (0 1 0) netplanes, see Fig. 1a. The structural description of MoO_3, as being built by weakly interacting tetrahedral chains, was confirmed by vibrational spectroscopy and by theory [66,67]. In this picture, the three types of oxygen centers the (0 1 0) surface are characterized by coordination spheres which are limited to shorter distances compared to the previous description. First, there are terminal Mo=O groups along the (0 1 0) direction, with oxygen coordinated to one molybdenum atom directly below/above at a distance of 1.67 Å. This is identical to the definition of O(1) in the previous description, see above. Second, the terminal Mo=O group along the (1 0 0) direction contains oxygen located asymmetrically between two Mo centers at a bonding distance of 1.73 Å and a 'non-bonding' distance of 2.25 Å. This oxygen corresponds to the asymmetric bridging O(2) in the previous description. Third, there is symmetric bridging oxygen along the (0 0 1) direction, placed symmetrically between two Mo centers of the surface layer with two bonding distances of 1.94 Å and linked to the second layer by a non-bonding distance of 2.33 Å. This is equivalent to O(3) of the previous description.

The MoO_3 crystal structure determines the geometry of local model clusters applied in surface studies. In previous theoretical MoO_3(0 1 0) surface studies [68–71] it has been found that cluster size convergence of electronic surface properties can be achieved with embedded clusters as large as $Mo_7O_{30}H_{18}$. In the present work a $Mo_{15}O_{56}H_{22}$ cluster, describing a bi-layer section of bulk MoO_3, is used to model the MoO_3(0 1 0) surface, see Fig. 2. This cluster contains all structurally different oxygen centers in their complete surface environment. Electronic embedding of the surface cluster is achieved by hydrogen terminators placed at the cluster periphery to saturate dangling oxygen bonds. The simulation of the local MoO_3(0 1 0) surface geometry by the $Mo_{15}O_{56}H_{22}$ cluster is tested by geometry optimizations in which all cluster atoms are allowed to rearrange except the peripheral hydrogen terminators. These optimizations

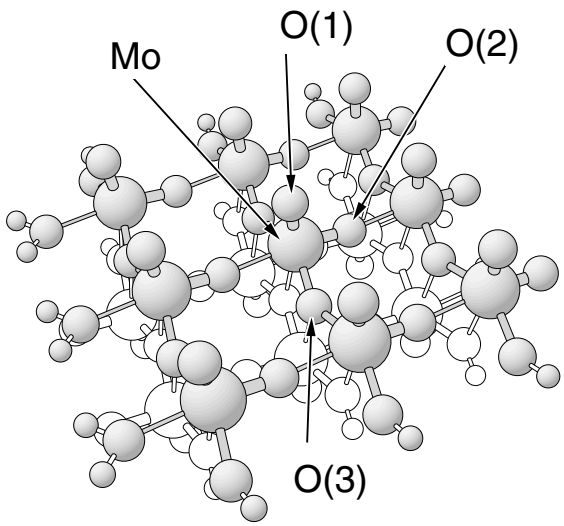

Fig. 2. Geometric structure of the $Mo_{15}O_{56}H_{22}$ cluster modeling a bi-layer section at the MoO_3(0 1 0) surface. Cluster atoms of the top (bottom) part of the bi-layer are shown as shaded (white) balls where the ball size decreases from Mo to O to H. The central molybdenum atom and its three neighboring non-equivalent surface oxygen centers, O(1–3), are labeled accordingly.

yield equilibrium positions for the surface atoms, which are very close to those of the bulk termination with inter-atomic distances varying by less than 0.05 Å.

Oxygen vacancies at the $MoO_3(0\,1\,0)$ surface are modeled by $Mo_{15}O_{56}H_{22}$–O vacancy clusters where '–O' means that an oxygen from one of the different surface sites O(1–3) has been removed from the clean $Mo_{15}O_{56}H_{22}$ substrate cluster (yielding in effect a $Mo_{15}O_{55}H_{22}$ cluster). Electronic properties of the vacancy clusters are obtained for the frozen surface geometry where all cluster atoms are fixed at their positions from the bulk termination. Calculations on the vacancy equilibrium geometries, where all cluster atoms are allowed to relax in response to the oxygen removal, are under way and will be reported elsewhere [72].

The electronic structure of the $MoO_3(0\,1\,0)$ surface clusters is determined by ab initio DFT where Kohn–Sham orbitals are represented by linear combinations of atomic orbitals (LCAOs). The LCAOs are described by extended all-electron (for O, H) and valence (for Mo) basis sets of contracted gaussians from atom optimizations [73,74] and the $[Ar]3d^{10}$ core of Mo is approximated by model core potentials [75]. Within the DFT framework electron exchange and correlation is described by gradient corrected functionals using the revised Perdew–Burke–Ernzerhof (RPBE) approach [76,77]. For all cluster calculations the program package DeMon [1] is employed. In addition to total energies and equilibrium geometries (based on numerical forces), detailed analyses of the electronic structure in the clusters are performed using Mulliken populations [78–81] and Mayer bond order indices [82,83]. Further, the dense energetic distribution of the Kohn–Sham valence levels in the present clusters allows the definition of a cluster total DOS, $n_{tot}(\varepsilon)$, and atom projected partial densities of states (PDOS), $n_A(\varepsilon)$, which are evaluated and can become useful in interpreting experimental photoemission spectra from the MoO_3 surface system as discussed below.

[1] The DFT-LCGTO program package DeMon was developed by A. St.-Amant and D. Salahub (University of Montreal). Here a modified version with extensions by L.G.M. Pettersson and K. Hermann is used.

2.2. Experimental

The different molybdenum oxides, MoO_2, Mo_4O_{11}, Mo_8O_{23}, and $Mo_{18}O_{52}$, are grown in a two-zone furnace by the CVT technique [84]. The temperature in the two different heating zones is controlled by Eurotherm (Syspro Cal 3200) temperature controllers. Molybdenum (Fluka, 99.7%, p.a.) and MoO_3 (Merck, p.a., heated for 30 min at 923 K) powder are chosen as source materials. Sealed silica transport tubes of 17.5 mm in diameter and 170 mm long are used where the mixed powders are loaded at one end. The tubes are heated with a flare gun at 2×10^{-4} mbar for $\approx$15 min and subsequently filled with argon. Re-sublimated $TeCl_4$, prepared from tellurium (Merck p.a.) and flowing chlorine in dried chlorine gas equipment, is used as transport agent. Re-sublimated iodine (Merck, 99.5%, p.a.) is used as transport agent for MoO_2. The transport agent is added (1 mg/ml) and the tubes are evacuated at 2×10^{-4} mbar and sealed off. The loaded transport tubes are put in the horizontal furnace and the sink is purified by a reverse transport step (see Table 1) for one day (for 14 days for MoO_2). The source is endothermically transported for four days (for 15 days for MoO_2). In order to avoid transport agent condensation on the crystal surfaces, a brief reverse transport step is carried out at the end of the experiment. The absence of transport agents at the surfaces is confirmed by energy-dispersive X-ray analysis (EDX), X-ray photoelectron spectroscopy (XPS) and ion scattering spectroscopy (ISS). After cooling to room temperature, the transport tubes are transferred to a glove bag filled with Ar in which the tubes are opened. For storage purposes, the samples are transferred to a glove box (MBraun, MB150 BGI, O_2 and $H_2O < 1$ ppm).

The molybdenum oxide, MoO_3, is also grown in a two-zone furnace by the CVT technique from MoO_3 powder (Merck, p.a., heated at 923 K, 30 min) as source material. After the cleaning procedure (vide supra), the fully oxidized MoO_3 powder is transported in a stream of water saturated synthetic air (3 ml/min) in a temperature gradient

Table 1
Transport parameters for the preparation of the molybdenum oxide phases MoO_2, Mo_4O_{11}, $Mo_{18}O_{52}$, and MoO_3[a]

Compound	MoO_x x	Transport agent (mg/ml)	Source temperature (K)	Sink temperature (K)	Duration (cleaning/CVT) (d)
MoO_2	2.00	3.9 (I_2)	1223	1123	14/15
m-Mo_4O_{11}	2.75	4.0 ($TeCl_4$)	923	873	1/4
$Mo_{18}O_{52}$	2.89	4.5 ($TeCl_4$)	1023	1003	1/4
MoO_3	3.00	105 Pa (H_2O/O_2)	923	823	1/4

[a] The transport procedure for MoO_3 was different than for the other materials. Therefore, the transport agent entry is in pressure units, Pa.

($T_2 = 923$ K, $T_1 = 823$ K) for four days. Cleaning, opening and storage is done as described above. The absence of impurities at the surface of the colorless crystals is confirmed by EDX, XPS and ISS. As an example, Fig. 3 displays the XP spectrum of a MoO_3 crystal for Mo 3d emission, which exhibits only two distinct single peaks ($3d_{3/2}$ and $3d_{5/2}$ emission). In addition, the inset of Fig. 3 shows the colorless MoO_3 crystal synthesized by the present preparation method. X-ray powder diffraction characterization, conducted on a Stoe StadiP diffractometer with a linear position sensitive detector in transmission mode (curved Ge (1 1 1) monochromator, Cu K_α radiation) confirms

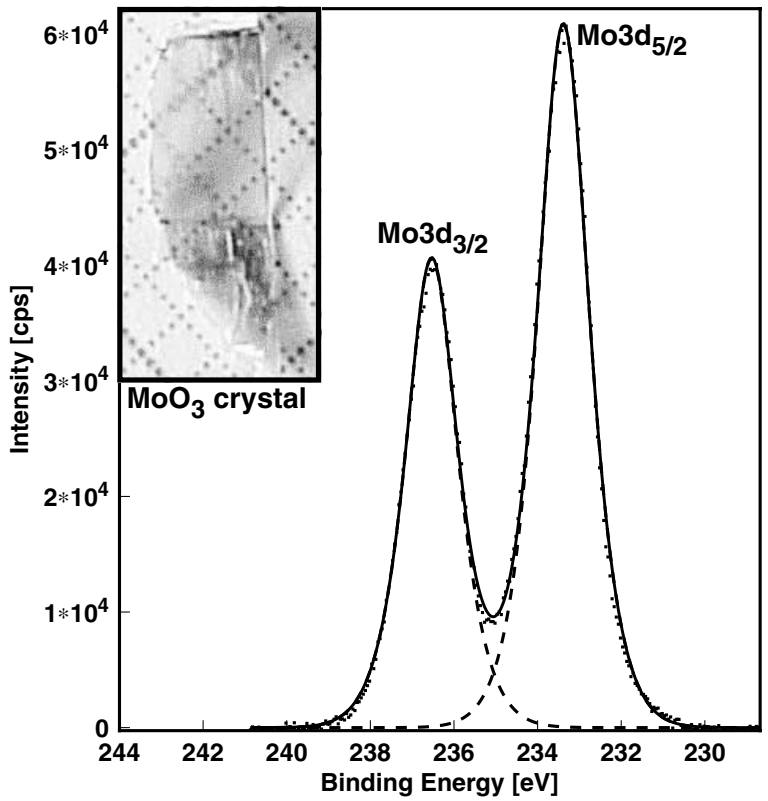

Fig. 3. Photoemission (XPS) spectrum of a MoO_3 crystal for Mo 3d emission exhibiting two distinct peaks ($3d_{3/2}$ and $3d_{5/2}$ emission). The inset at the left top shows the colorless MoO_3 crystal synthesized by the present preparation method.

the structure of the synthesized crystals. The diffraction patterns are evaluated in a 2θ range between 5° and 105° in agreement with the literature.

Surface analysis is performed with a combined XPS–UPS–ISS instrument (Leybold-Heraeus), using Mg K_α X-ray radiation (150 W), with an EA 200 hemispherical analyzer at a band pass energy of 48 eV resulting in 1.0 eV resolution. The XPS binding energy scale is calibrated with Au 4f emission at 84 eV and Cu 2p emission at 932.7 eV. The data are analyzed using satellite and Shirley background subtraction. The crystals are mounted on stainless steel sample holders. Surface purity after the Chemical Transport and full oxidation of the surface is confirmed by XPS. Fig. 3 shows the Mo 3d XP spectrum prior to the UPS/ISS experiments. Surface reduction to Mo^{5+} or Mo^{4+} could not be detected above the detection level. He I (21.22 eV) and He II (40.85 eV) UV radiation is used for UPS with a band pass energy of 6 eV and an angle of 65° between the sample normal and the UV lamp. Since stoichiometric MoO_3 is an insulator, the reference spectrum of the sample holder is used for the determination of the Fermi level. The work function of the samples is evaluated by subtracting the difference between high and low energy cutoffs from the photon energy. Ion surface sputtering (ISS) is performed with He^+ ions at 1 keV and an ion current of 1 nA, giving a flux of 6×10^{12} ions/cm^2 per scan.

3. Results and discussion

3.1. Electronic structure of the $MoO_3(0\,1\,0)$ surface

Table 2 lists geometric and electronic parameters of the $Mo_{15}O_{56}H_{22}$ cluster which is found to be large enough to yield a meaningful description of the $MoO_3(0\,1\,0)$ surface. Results of atom charges q(A) (from Mulliken populations) and bond orders p(A–B) (Mayer bond order indices) are given for selected atoms closest to the cluster center. In addition, Kohn–Sham level energies of the highest occupied orbitals (HOMOs) are included. The computed data are given for the cluster geometry taken from the experimental bulk geometry [56] (second column of Table 2) as well as for the cluster where all atom positions except for the hydrogen terminators are optimized according to lowest total energy (third column). A comparison of the results for the two geometries shows only minor differences that are too small to be physically/chemically relevant. The populations show that, in agreement with chemical intuition, all molybdenum atoms are positively charged and all oxygen atoms are negative in the clusters. The molybdenum centers are described as $Mo^{2.2+}$ ions with minor charge variation ($\Delta q = 0.2$) inside the cluster. The negative oxygen charges amount to -0.5 for singly coordinated terminal oxygen O(1), -0.7 for doubly coordinated (asymmetrically) bridging oxygen O(2), and -1.0 for triply coordinated (symmetrically) bridging oxygen O(3), and, therefore, scale with coordination. This result indicates that the largest ionic contributions to interatomic binding at the $MoO_3(0\,1\,0)$ surface involve the symmetrically bridging O(3) oxygen sites. Clearly, local charging of the different cluster atoms is found to be much smaller than formal valence charges, Mo^{6+} and O^{2-}, of a fully ionic MoO_3 compound would suggest. Apart from the arbitrariness of assigning charge to single atom centers in a compound system and the uncertainty of the charge evaluation using Mulliken popula-

Table 2
Selected atom charges q(A), bond orders p(A–B), distances $d_{O\text{–}Mo}$, and HOMO energies ε_{HOMO} of the $Mo_{15}O_{56}H_{22}$ cluster representing $MoO_3(0\,1\,0)$ surface[a]

	Bulk termination	Optimized cluster
q(Mo)	2.23	2.16
q(O(1))	−0.48	−0.48
q(O(2))	−0.74	−0.72
q(O(3))	−0.99	−0.97
p(O(1)–Mo)|$d_{O\text{–}Mo}$ (Å)	1.66|1.67	1.74|1.69
p(O(2)–Mo)|$d_{O\text{–}Mo}$ (Å)	1.05|1.73	1.13|1.75
	0.33|2.25	0.31|2.33
p(O(3)–Mo)|$d_{O\text{–}Mo}$ (Å)	0.26|1.94	0.28|1.97
	0.44|1.94	0.45|2.03
	0.31|2.33	0.32|2.28
ε_{HOMO} (eV)	−6.14	−6.64

[a] The results refer to DFT calculations using the RPBE approximation. The data are given for the cluster with bulk termination as well as for the cluster where all atom positions are optimized according to lowest total energy, see text.

tions, the present results indicate that inter-atomic binding in MoO_3 is described by both ionic and sizeable covalent contributions.

Covalent contributions to Mo–O binding can be estimated roughly from corresponding bond order indices. The data of Table 2 confirm the general picture based on simple valence concepts revealing three types of Mo–O bonds. Bonds between terminal (molybdenyl) oxygen, O(1), and molybdenum yield bond order values of 1.7, i. e. close to 2, which suggests double bonds and is consistent with the single coordination of O(1). Asymmetrically bridging oxygen O(2) binds to two neighboring Mo centers with bond order values of 1.0 for the center at closer and 0.3 for that at further distance, corresponding to one single and one much weaker bond which is reasonable in view of the environmental geometry of O(2). Symmetrically bridging oxygen O(3), which is coordinated to three neighboring Mo centers (two of the upper and one of the lower part of the bi-layer), yields bond order values of 0.3–0.4 indicating three bonds which are similar in strength and considerably weaker than single bonds. This analysis shows, in particular, non-negligible bond orders of about 0.3 for Mo–O bonds with long inter-atomic distances appearing for both symmetric and asymmetric oxygen (and neglected in the description of MoO_3 by tetrahedra chains). Therefore, the concept of MoO_3 consisting of coupled MoO_6 octahedra seems to be more appropriate to account for the electronic structure of the system. If the sum of bond orders, Σ, of each oxygen center with its Mo neighbors is taken as the total amount of its covalent binding the highest value is obtained for O(1) ($\Sigma = 1.7$), followed by O(2) ($\Sigma = 1.4$) and O(3) ($\Sigma = 1.0$). This correlates nicely with the increase in negative charge from O(1) to O(2) to O(3). Altogether, the results suggest for the different oxygen centers at the $MoO_3(0\,1\,0)$ surface that an increase in coordination with respect to Mo neighbors leads to an increase in ionic binding character for the oxygen but is combined with a decrease of its covalent binding.

Table 2 contains also Kohn–Sham level energies ε_{HOMO} of the HOMO of the $Mo_{15}O_{56}H_{22}$ cluster. Based on general DFT theory [73] the quantity $-\varepsilon_{HOMO}$ represents the first cluster ionization potential which will converge with increasing cluster size towards the workfunction of the $MoO_3(0\,1\,0)$ surface. In this spirit, the calculated values $-\varepsilon_{HOMO}$ represent a 'cluster workfunction' of 6.1 eV (bulk termination) and 6.6 eV (optimized cluster). This value is quite close to the experimental workfunction for $MoO_3(0\,1\,0)$ estimated from the present photoemission data which amounts to 6.1 eV. It is also reasonable in view of typical workfunction values of transition metal oxide surfaces, e.g. 6.4 ± 0.7 eV for $V_2O_5(0\,1\,0)$ [85]. The character of the HOMO and lowest unoccupied orbitals (LUMO) of the $Mo_{15}O_{56}H_{22}$ cluster, separated by about 2 eV in the calculations, can be obtained from population results. The analysis shows that the HOMO is described by dominant oxygen 2sp contributions while the LUMO can be characterized by molybdenum 4d contributions. This indicates that optical absorption leading to electronic HOMO–LUMO excitations is combined with oxygen to metal charge transfer at the surface. Further, adding electronic charge to the surface, e.g. by adsorbate induced charge transfer, will result in increased 4d occupation of the metal ions at the surface which can be related to chemical reduction.

The electronic structure of the $Mo_{15}O_{56}H_{22}$ cluster can also be characterized by energy level distributions of the occupied Kohn–Sham valence orbitals. The rather dense distribution of valence orbitals as a consequence of the cluster size makes the definition of total and partial densities of states (DOS/PDOS) meaningful as mentioned already in Section 2.1. As a result, Fig. 4 shows corresponding DOS and PDOS curves calculated for the $Mo_{15}O_{56}H_{22}$ cluster with bulk termination where a gaussian level broadening of 0.4/1.0 eV (Fig. 4a–c) is applied. (The two different broadening values are used to analyze the data in detail at reasonably high resolution (0.4 eV) and to compare directly with experiment which yields a resolution of 1.0 eV.) The energetic position of the highest occupied cluster orbital ε_{HOMO} at -6.1 eV is marked by a thin vertical line. Fig. 4a gives the total DOS curve for the valence band region of the cluster together with its decomposition into molybdenum and oxygen contributions while in Fig. 4b the PDOS curves of the differently coordinated oxygen centers O(1–3) are displayed. In addition,

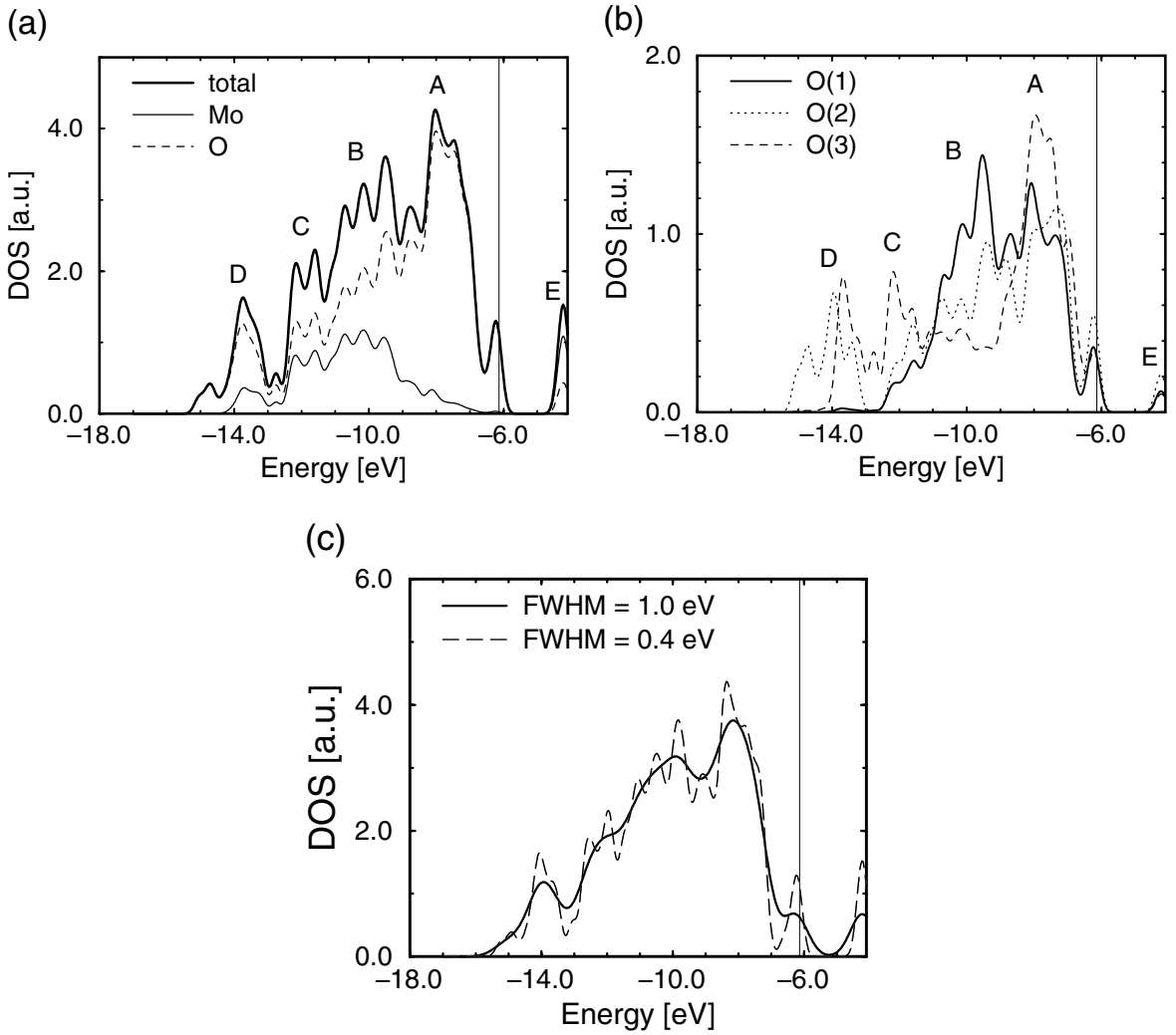

Fig. 4. Total and atom projected partial densities of states (DOS/PDOS curves) of the valence band region calculated for the $Mo_{15}O_{56}H_{22}$ cluster. DOS values refer to atomic units while energies are given in eV. The energetic position of the highest occupied cluster orbital ε_{HOMO} at −6.1 eV is marked by a thin vertical line. (a) Total DOS curve (thick solid) with decomposition into molybdenum (thin solid) and oxygen (dashed) contributions. (b) PDOS curves of the differently coordinated oxygen centers O(1) (solid), O(2) (dotted), and O(3) (dashed). In figures (a) and (b) a gaussian level broadening of 0.4 eV is applied. (c) Total DOS curves for a level broadening of 0.4 eV (dashed) and 1.0 eV (solid) where the latter reflects the resolution in the UPS measurements.

Fig. 4c compares the total DOS for different level broadening, 0.4 and 1.0 eV. The valence band region, which extends from −12.5 to −6.1 eV, is described by a DOS of multi-peak structure (regions A–C) where the decomposition shows clearly that dominant contributions are due to oxygen while molybdenum contributions are smaller and confined to the lower part of the valence band region. Population analyses identify the oxygen contributions as O 2sp and those due to molybdenum as Mo 4d which is to be expected based on the valence configuration of the atoms and their formal valence in MoO_3 bulk. The additional set of levels between −15.0 and −12.8 eV (region D, below the valence band region), which is due to split-off orbitals as a consequence of the

bond saturation at the cluster periphery, has to be considered a cluster artifact. The valence band region assumes a width of $\Delta = 6.4$ eV in the present $Mo_{15}O_{56}H_{22}$ cluster which is rather close to the total valence band width of the extended $MoO_3(0\,1\,0)$ surface system. This is confirmed by comparisons with recent MoO_3 bulk and (0 1 0) slab [65] calculations, yielding valence band widths of $\Delta = 6$–7 eV [64,65], as well as with the experimental He II photoemission data for $MoO_3(0\,1\,0)$ [62] discussed below.

The valence band region can be characterized in more detail based on the PDOS curves shown in Fig. 4b where the oxygen PDOS is decomposed further according to the differently coordinated surface oxygen sites O(1–3). The total DOS curve allows the distinction of three main peak regions A–C where the energetically highest region A (about 2 eV below the upper valence band edge, ε_{HOMO}) is described by contributions from oxygen of all three coordination types with that of O(3) being most pronounced. The central region B (about 4 eV below ε_{HOMO}) is characterized by oxygen with dominating O(1) contributions in addition to small molybdenum admixtures. The lowest region C (about 5.5 eV below ε_{HOMO}) has dominant O(3) as well as molybdenum character. The region E of unoccupied levels, representing the bottom of the conduction band region of the substrate within the cluster approach, starts at 1.8 eV above the upper valence band edge which is consistent with the well-known experimental result of bulk MoO_3 forming a small band gap insulator [1]. The computed gap size of 1.8 eV is smaller than experimental values (3.2–3.4 eV), derived from photoabsorption measurements. This is explained by the well-known deficiency of DFT to describe occupied and unoccupied electron levels by the same functional, which results always in gap values which are too small [86]. Fig. 4a shows in addition that the lower part of region E is dominated by molybdenum contributions which are described as Mo 4d type based on an orbital analysis. This confirms the rough qualitative picture of the electronic structure of MoO_3 being described by a conduction band region of dominant Mo 4d type in addition to the O 2sp type valence band region.

The surface cluster approach uses local clusters whose geometries reflect those of finite sections cut out of the real substrate surface. This implies, in particular, that the equilibrium geometry of the surface cluster describes that at the real surface to a good approximation. The quality of this approach and its consequence for the electronic structure can be tested by full geometry optimizations carried out for the surface cluster. In the present work, the $Mo_{15}O_{56}H_{22}$ cluster is optimized by allowing all cluster atoms, except for peripheral hydrogen terminators, to relax according to lowest cluster total energy. This optimization yields a total energy lowering of only 4.26 eV compared to total energies of 142 keV. The rightmost column of Table 2 lists geometric and electronic parameters of the optimized cluster. A comparison of the corresponding data for the two cluster geometries in Table 2 evidences that the optimization results in differences which are overall small and justify the use of both clusters to represent the extended $MoO_3(0\,1\,0)$ substrate surface.

3.2. Oxygen vacancies at the $MoO_3(0\,1\,0)$ surface

The three different types of surface oxygen vacancies which exist at the ideal $MoO_3(0\,1\,0)$ surface are modeled by the $Mo_{15}O_{56}H_{22}$–O (=$Mo_{15}O_{55}H_{22}$) cluster, cp. Section 2.1, where oxygen is removed from one of the three surface sites O(1–3) as indicated in Fig. 5. In the present calculations the oxygen is removed and the electronic structure of the vacancy cluster is evaluated with its atoms kept fixed at their positions of the bulk termination ('frozen vacancy cluster'). Oxygen vacancy formation energies, $E_D^f(O)$ are then calculated from corresponding cluster and atomic total energies as

$$E_D^f(O) = |E_{tot}^f(Mo_{15}O_{56}H_{22}\text{–}O) + E_{tot}(O) - E_{tot}^f(Mo_{15}O_{56}H_{22})| \quad (1)$$

where $E_{tot}^f(Mo_{15}O_{56}H_{22})$ and $E_{tot}(O)$ are ground state total energies of the cluster without vacancy and of the neutral oxygen atom, respectively, and $E_{tot}^f(Mo_{15}O_{56}H_{22}\text{–}O)$ refers to the frozen vacancy cluster.

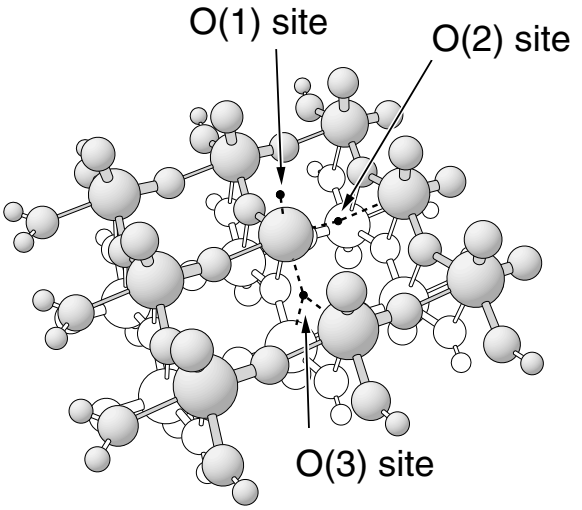

Fig. 5. Sketch of the vacancies at different surface oxygen sites O(1–3) in the $Mo_{15}O_{56}H_{22}$ cluster. Cluster atoms of the top (bottom) part of the bi-layer are shown as shaded (white) balls where the ball sizes decrease from Mo to O to H. The vacancies are sketched as black dots.

Table 3 lists formation energies $E_D^f(O)$ obtained by the present calculations using the DFT scheme together with the RPBE functional. Here $E_D^f(O)$ is the largest, 7.6 eV, for the singly coordinated terminal O(1) site, cp. Fig. 5, while for the two bridging sites, O(2) and O(3), somewhat smaller values, 7.1 and 6.8 eV, are obtained. Experimental data of oxygen vacancy formation energies in MoO_3 do not seem to be available for comparison. The $E_D^f(O)$ values are very similar to findings for oxygen vacancies at the vanadium pentoxide surface, $V_2O_5(0\,1\,0)$, where formation energies of 7–8 eV have been calculated [86,87]. Thus, the present data suggest that oxygen vacancy energies are rather large for all surface sites, which makes it quite difficult to remove oxygen by itself from the ideal $MoO_3(0\,1\,0)$ surface. This result is in agreement with in situ Raman data on the ^{18}O exchange in MoO_3, which does not happen for stoichiometric MoO_3. Only reduced MoO_{3-x}, containing oxygen vacancies, can be re-oxidized [88]. Furthermore, in line with the theoretical data, the in situ experiments show that the degree of ^{18}O-incorporation scales with the Mo–O bond order, i.e. the lower the bond order, the higher the degree of ^{18}O-labeling.

Table 3
Vacancy formation energies, $E_D^f(O)$, of the different oxygen surface sites O(1–3), for definitions see text[a]

Site	$E_D^f(O)$ (eV)
O(1)	7.64
O(2)	7.09
O(3)	6.81

[a] The data are obtained from DFT calculations using the RPBE functional where a local section at the $MoO_3(0\,1\,0)$ surface is modeled by a $Mo_{15}O_{56}H_{22}$ cluster. Energy values are given in eV.

Based on the present theoretical results, oxygen insertion in an oxidation reaction at the $MoO_3(0\,1\,0)$ surface must proceed in a concerted fashion which avoids removal of oxygen by itself from the unperturbed surface in a single step. Possible scenarios include lowering of the oxygen desorption energy by surface imperfections (e.g. existing oxygen vacancies), by the influence of the adsorbed reactant, or by pre-adsorption of atoms or molecules at the oxygen site. The latter possibility has been discussed in theoretical studies for oxygen desorption from the $MoO_3(0\,1\,0)$ [72,89] and $V_2O_5(0\,1\,0)$ surface [90,91] where pre-adsorption of hydrogen at the oxygen site followed by desorption of OH groups was found to be energetically favorable over direct oxygen desorption.

Table 4 lists selected atom charges q(A) and bond orders p(A–B) of the clusters $Mo_{15}O_{56}H_{22}$–O representing the different oxygen vacancies O(1–3) at the $MoO_3(0\,1\,0)$ surface (frozen cluster geometries, see above). For comparison, this table contains also corresponding results for the vacancy free $Mo_{15}O_{56}H_{22}$ cluster with bulk termination (denoted 'substrate'), taken from Table 2. A closer inspection of the atom charges of Table 4 reveals that the positive charges of the central molybdenum atoms closest to each oxygen vacancy are smaller than corresponding values in the cluster without vacancy, where charge differences amount to 0.5–0.9 electrons. This charge decrease can be explained by the fact that the vacancy oxygen was a negatively charged species at the surface. Therefore, when the oxygen is removed to yield a neutral final product it leaves a negative excess charge behind, which is distributed over the atoms

Table 4
Selected atom charges q(A) and bond orders p(A–B) of the $Mo_{15}O_{56}H_{22}$–O clusters representing the different oxygen vacancies O(1–3) at the MoO_3(0 1 0) surface[a]

	O(1) vac.	O(2) vac.	O(3) vac.	Substrate
q(Mo)	1.57	1.32	1.70	2.23
q(O(1))	–	−0.46	−0.48	−0.48
q(O(2))	−0.66	–	−0.73	−0.74
q(O(3))	−0.96	−0.96	–	−0.99
p(Mo–O(1))	–	1.97	1.75	1.66
p(Mo–O(2))	1.45	–	1.11	1.05
	0.22		0.31	0.33
p(Mo–O(3))	0.46	0.36	–	0.26
	0.44	0.46		0.44
	0.28	0.29		0.31

[a] The results refer to DFT calculations using the RPBE functional and the frozen cluster geometry, see text. The results for the $Mo_{15}O_{56}H_{22}$ cluster with bulk termination (denoted 'substrate') are taken from Table 2 and are included for comparison.

close to the vacancy and compensates some of the positive metal charge. This is a simple microscopic picture of chemical reduction of the metal sites near the oxygen vacancies. In contrast to the sizeable charge reduction of the metal atoms, the oxygen atoms near the vacancy experience only small changes in their charge state. In all cases, oxygen atoms become less negative, however, with charge differences below 0.1 electrons. A comparison of the bond order results for the different oxygen vacancy clusters with those of the vacancy-free cluster shows that the largest effect occurs when the O(1) vacancy is created. Here the bond order between the central Mo center of the asymmetric bridging oxygen O(2) increases by almost 40% suggesting a Mo–O(2) bond strength near the O(1) vacancy which is similar to that of the original Mo–O(1) bond. Thus, in terms of Mo–O binding the asymmetric bridging oxygen O(2) takes the place of the original terminal O(1) atom which has been removed in the vacancy creation process. This finding may become important for the vacancy properties when surface relaxation is included in the vacancy calculation [72].

An alternative view of the chemical reduction effect at the metal sites near the oxygen vacancies becomes possible by atom projected PDOS and orbital analyses of the vacancy clusters. As an example, Fig. 6 shows DOS and PDOS curves of the valence band region obtained for the $Mo_{15}O_{56}H_{22}$–O cluster with a triply coordinated oxygen vacancy O(3). In Fig. 6a, the total DOS (thick

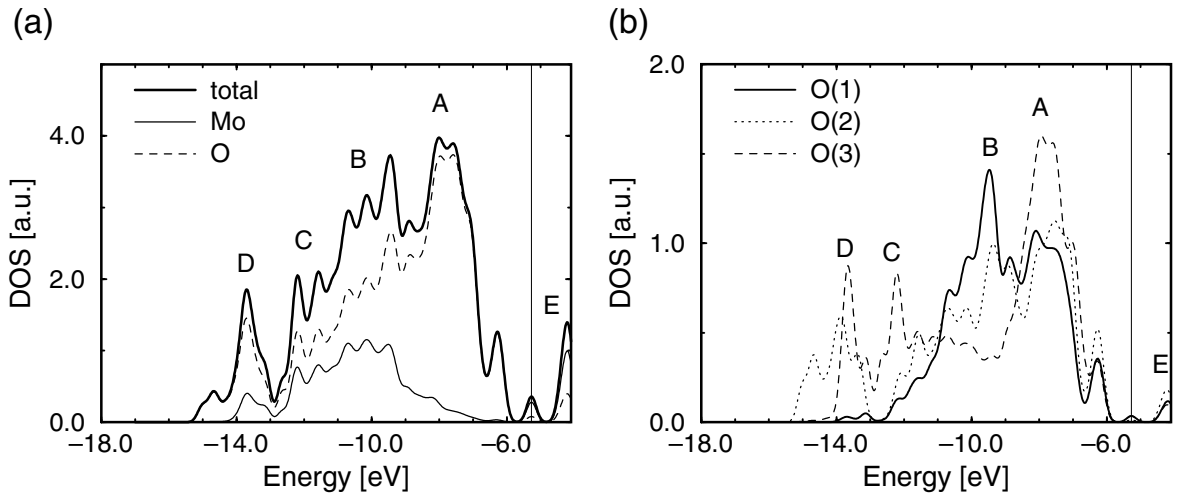

Fig. 6. Total and atom projected partial DOS/PDOS curves of the valence band region for the $Mo_{15}O_{56}H_{22}$–O cluster with a triply coordinated oxygen vacancy O(3). (a) Total DOS curve (thick solid) with decomposition into molybdenum (thin solid) and oxygen (dashed) contributions. (b) PDOS curves of the differently coordinated oxygen centers O(1) (solid), O(2) (dotted), and O(3) (dashed). In both figures a gaussian broadening of 0.4 eV is applied. DOS values refer to atomic units while energies are given in eV. The energetic position of the highest occupied cluster orbital ε_{HOMO} at −5.3 eV is marked by a thin vertical line.

line) is decomposed in molybdenum (thin) and oxygen (dashed) PDOS contributions while in Fig. 6b the oxygen derived PDOS of Fig. 6a is further separated into contributions originating from the differently coordinated oxygen sites O(1–3). In both figures a gaussian level broadening of 0.4 eV is applied and the energetic position of the highest occupied cluster orbital ε_{HOMO} at −5.3 eV is indicated by a thin vertical line. A detailed comparison of Fig. 6 with Fig. 4 (giving the (P)DOS results of the vacancy-free cluster) shows only very small differences over the whole range of the oxygen 2sp dominated valence band region except for its upper edge. In this region near the HOMO at −6.1 eV the occupied orbitals of the vacancy-free cluster are determined by O 2sp contributions whereas in the vacancy cluster the HOMOs (below 5.3 eV) are characterized as Mo 4d type. An analysis of these metal derived valence orbitals (which are unoccupied in the vacancy-free cluster) reveals further that their charge distribution is located mainly at the three Mo sites adjacent to the vacancy. Thus, the calculations show that the oxygen vacancy leads to increased local molybdenum 4d occupation. This result was also found in the (P)DOS and orbital analyses of the other vacancy clusters (describing O(1) and O(2) vacancy sites) and confirms the picture of chemical reduction of adjacent metal centers induced by the oxygen vacancies and observed already in the population results.

Valence photoemission spectra from substrate surfaces are, apart from transition matrix elements, determined by the DOS of the corresponding valence electron states. Therefore, the present findings of additional occupied states of Mo character located above the O 2sp derived valence region are relevant for the interpretation of experimental photoemission spectra of molybdenum oxide surfaces. According to the present calculations, additional photoemission intensity above the valence band region may be indicative of chemical reduction of the metal centers (leading to lower oxidation states) where the effect can be introduced by oxygen vacancies or by different chemical composition of the oxide. This will be discussed in more detail in the next section.

The present cluster calculations ignore an important contribution in the vacancy formation, which is connected with the fact that the equilibration process, induced by the oxygen removal, leads to a geometric rearrangement (relaxation) of the surrounding surface atoms. This can be accounted for by vacancy cluster calculations where all cluster atoms are allowed to equilibrate. Calculations along these lines are presently under way where preliminary test results indicate [72] that the qualitative findings obtained with the frozen vacancy clusters of this work do not change. This is consistent with earlier results from cluster model studies on oxygen vacancies at the $V_2O_5(0\,1\,0)$ surface where vacancy formation energies are reduced by 0.5–1.0 eV due to surface relaxation but electronic parameters are affected much less. In test calculations local electronic states at oxygen vacancies have been studied by including additional orbital basis sets at the vacancy sites. The calculations do not yield any low-lying electron states localized at the vacancies and reminiscent of color centers. This can be rationalized by simple geometric arguments based on the size of the surface vacancies at $MoO_3(0\,1\,0)$ and by the strength of the electrostatic Madelung potential near the vacancies which is analogous to the case of oxygen vacancies at the $V_2O_5(0\,1\,0)$ surface [91].

3.3. Photoemission on molybdenum oxide surfaces

Fig. 7a shows He II photoemission spectra obtained for a series of well-crystallized (single-phase) molybdenum oxides with stoichiometries between MoO_3 and MoO_2. Fully stoichiometric MoO_3 does not exhibit a He II photoemission spectrum as expected for an insulator. Valence band emission can be recorded only after prolonged exposure to UHV and intensity in the band gap region cannot be observed for MoO_3 as expected for a stoichiometric oxide. The appearance of a Fermi edge (Fig. 7b and c) is due to spurious emission from the steel sample holder. The work function for $MoO_3(0\,1\,0)$ is determined experimentally to be 6.1 eV which compares well with the calculated value of 6.1–6.6 eV. The widths of the valence bands are between 6 and 8 eV for MoO_3 and about 10 eV for MoO_2. This result

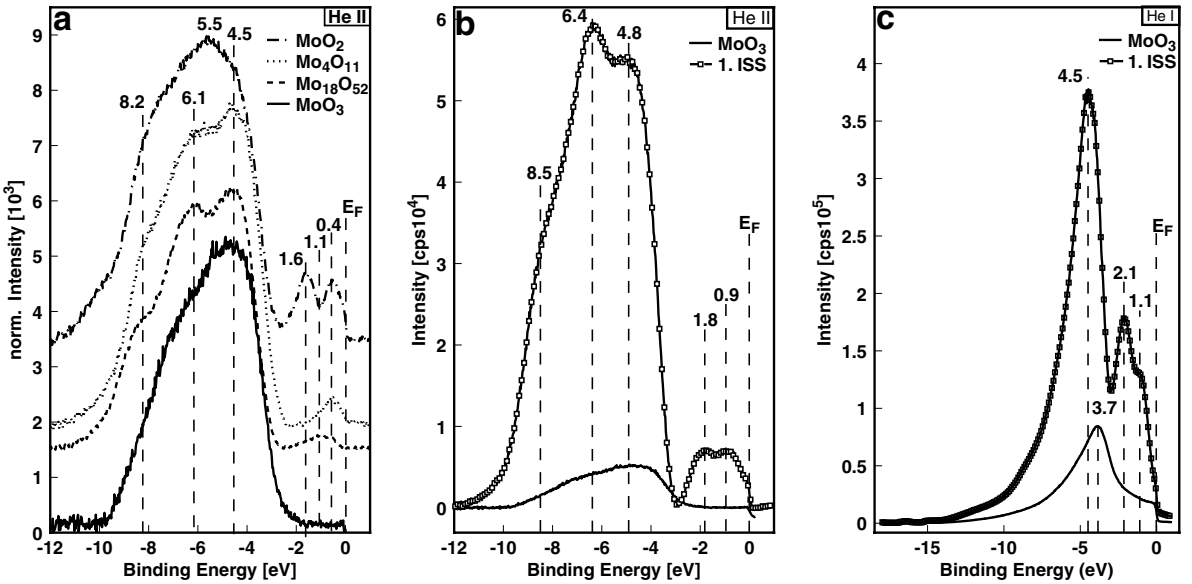

Fig. 7. Experimental photoemission spectra of different molybdenum oxide samples. (a) He II spectra for single crystal MoO_2, MoO_3, and for well-crystallized intermediate molybdenum oxides, Mo_4O_{11}, $Mo_{18}O_{52}$. (b) He II spectra for single crystal MoO_3 before (full line) and after mild ion bombardment (with squares). (c) He I spectra for single crystal MoO_3 before (full line) and after mild ion bombardment (with squares).

compares well with the theoretical values for the $Mo_{15}O_{56}H_{22}$ and $Mo_{15}O_{55}H_{22}$ clusters as well as with literature values of 6–7 eV [64,65]. The changes in the shape of the valence band spectra in this series of oxides can be explained on the basis of the above-discussed calculations. After prolonged exposure to the UHV, the photoemission spectrum of fully stoichiometric MoO_3 reveals a valence band structure with a peak at 4.5, and a shoulder at 6.1 eV. These peaks can be assigned to contributions of the three different oxygen species. Hence, the peak at 4.5 eV arises mainly from contributions due to the bridging O(3) species (oxygen in (0 0 1) direction of the MoO_4-chains), whereas the peak at 6.1 eV is mainly due to the terminal oxygen O(1) with the shortest bond length and highest bond order.

Reduction of MoO_3 and formation of $Mo_{18}O_{52}$ leads to the appearance of a new peak in the band gap at 1.1 eV below the Fermi level which is attributed to 4d contributions of reduced Mo centers. In addition, changes in the O 2sp valence spectra, a relative increase in the peak height at 6.1 eV compared to that at 4.5 eV, are observed. This can be understood on the basis of the calculations as the preferential loss of bridging oxygen O(3). This finding is in agreement with in situ Raman results on ^{18}O incorporation into MoO_{3-x} [88] and the reduction of MoO_3 to hydrogen bronzes [92] which also reveal preferential loss of bridging oxygen.

Further reduction to Mo_4O_{11} leads to a shift of the defect state in the band gap toward the Fermi level with its maximum at 0.4 eV and to an increase of its intensity as can be expected due to the higher degree of reduction. MoO_2 gives rise to a UV photoemission spectrum with two Mo defect states below the Fermi level at 0.4 and 1.6 eV, which is in line with the known two different Mo^{4+} sites the MoO_2 lattice. The relative intensity of this doublet is enhanced in comparison with that of the single peaks for Mo_4O_{11} or $Mo_{18}O_{52}$, indicating the higher degree of reduction of MoO_2. The peak at 4.5 eV remains as a shoulder whereas the former peak at 6.1 eV shifts to 5.5 eV in MoO_2. These changes may be interpreted again as due to

preferential loss of bridging oxygen but also to structural differences between the MoO_3 and the MoO_2 crystal lattices.

Fig. 7b and c show the He II and He I photoemission spectra obtained for MoO_3 after evacuation to UHV and subsequent gentle ion bombardment. Fig. 7c depicts the He I photoemission spectrum of stoichiometric and of ion sputtered MoO_3. The He I photoemission spectrum of pristine MoO_3 could not be determined. The structure-less spectrum shown in Fig. 7c is due to a strongly insulating material and contains contributions from ghost emission of the surrounding sample holder as indicated by the Fermi edge. The O 2sp emission is observed at 3.7 eV, at lower energies as compared to 4.8 eV in the He II spectrum (Fig. 7b). However, this shift is artificial and due to the strongly insulating properties of the MoO_3 sample which are also indicated by the exponential intensity decay toward higher energies.

Ion bombardment is frequently used in UHV experiments for surface cleaning. Considerable spectral changes are observed in the photoemission spectra. Fig. 7b also shows the He II spectra after mild ion bombardment of stoichiometric MoO_3. The width of the valence band is increased to about 10 eV for the ion sputtered oxide as compared to stoichiometric MoO_3 (7 eV). This result is consistent with the increased theoretical value of about 8 eV for the $Mo_{15}O_{56}H_{22}$–O cluster. Already after the first ISS scan, two additional Mo contributions are detected in the band gap at 0.9 and 1.8 eV. The position and the shape of these two additional peaks point to an ISS induced reduction of surface Mo ions by an amount comparable to that of MoO_2. The calculations, however, do not produce such a twin peak in the band gap upon the generation of an oxygen vacancy. Thus, it must be concluded that the gentle ion bombardment already leads to a considerable surface damage.

The observation of surface reduction by ISS is confirmed by the changes in the O 2sp valence band emission exhibiting peaks or shoulders at 4.8, 6.4 and 8.5 eV, see Fig. 7b. The shape of the photoemission spectrum after ion bombardment is comparable to those of the He II spectra of the reduced molybdenum oxides, $Mo_{18}O_{52}$, Mo_4O_{11} and MoO_2 (Fig. 7a). As discussed above for the latter oxides, the changes in the O 2sp valence spectra can be understood on the basis of the calculations as preferential loss of bridging oxygen.

The He I valence band emission of MoO_3 can also be recorded after gentle ion bombardment, see Fig. 7c. In comparison with He II, He I excitation is accompanied by a higher cross-section of the Mo 4d states relative to the O 2sp states. Thus, the spectrum of the ion sputtered MoO_3 exhibits a stronger Mo 4d emission at 1.1 and 2.1 eV relative to the oxygen emission detected at 4.5 eV if the He I spectrum is compared with that for He II emission (Fig. 7b). As discussed before for the He II spectrum, the two peaks at 1.1 and 2.1 eV indicate reduction of the Mo centers.

In summary, it is possible to measure photoemission spectra of a series of molybdenum oxides between MoO_3 and MoO_2. The photoemission of MoO_3 can only be recorded after prolonged exposure to UHV, which presumably induces surface conductivity due to oxygen loss, i.e. non-stoichiometry. The changes in shape of the photoemission spectra within this series of molybdenum oxides can be interpreted on the basis of the cluster calculations as the preferential loss of more weakly bound, bridging oxygen. The increasing degree of reduction also leads to new photoemission peaks in the band gap due to reduced Mo species. The position and number of emission peaks depends on the degree of reduction. Gentle ion bombardment – often used in UHV studies for surface cleaning – induces surface reduction of MoO_3 and leads to spectral changes comparable to those observed for the reduced molybdenum oxides. Hence, care has to be taken when attempting to generate or treat molybdenum oxide surfaces by typical UHV cleaning procedures.

4. Conclusions

The present ab initio DFT cluster studies together with experimental photoemission results can provide rather detailed information about the electronic structure of the $MoO_3(0\,1\,0)$ surface as well as about electronic structure changes due to formation of surface oxygen vacancies. The

calculations on embedded clusters as large as $Mo_{15}O_{56}H_{22}$ confirm the mixed covalent/ionic character of the oxide. They suggest in addition that the concept of MoO_3 consisting of coupled MoO_6 octahedra is more appropriate to account for the electronic structure of the system compared with a description by coupled tetrahedra. Further, the computed width of the O 2sp dominated valence band region of MoO_3, about 7 eV, agrees well with the present and previous photoemission data for carefully prepared $MoO_3(0\,1\,0)$ samples. The experimental and calculated work functions also agree well with 6.1 eV (experiment) and 6.1–6.6 eV (theory). The overall shape of the computed DOS curve of the O 2sp region of MoO_3 is rather similar to the measured He II UPS intensity curves if the same spectral resolution (1.0 eV) is considered (cp. Fig. 4c). This indicates weak energy dependence of corresponding transition matrix elements. The calculations of vacancy energies for the different surface oxygen sites at $MoO_3(0\,1\,0)$ (neglecting surface relaxation) yield rather large values, 6.8–7.6 eV. This shows that oxygen is bound quite strongly to the substrate and may not be easily removed by itself from the surface. Vacancy formation leads to chemical reduction of neighboring molybdenum centers which expresses itself by increased metal d electron occupation and corresponding DOS contributions above the O 2sp region. This is consistent with the experimental UPS data for $MoO_3(0\,1\,0)$ where oxygen vacancies have been introduced by mild ion bombardment. It is further supported by the present UPS data for well-crystallized intermediate molybdenum oxides, such as $Mo_{18}O_{52}$, Mo_8O_{23}, or Mo_4O_{11}. A comparison of theory and experiments indicates that the spectral changes with increasing degree of reduction are induced by preferential loss of bridging oxygen. Mild ion bombardment, a technique which is often used to clean surfaces in UHV experiments, results, in the case of $MoO_3(0\,1\,0)$, in considerable surface reduction. Therefore, this technique cannot be considered a suitable tool for the preparation of stoichiometric molybdenum oxide surfaces.

With respect to elucidating the function of selective oxidation catalysts this study has corroborated earlier results drawing upon the defective nature of genuine crystal surfaces. It was possible to relate the evolution of reduced states of Mo in to specific crystallographic structures. The speculation of the surface oxygen defects as bridging sites raises the question about a restructuring of a defective surface which may no longer be described as a cut through a bulk orientation. Before this aspect can be elucidated further, the study needs to reproduce the present findings in systems containing at least one of the essential promoter elements required for mimicking the practically observed function of the oxide. This is possible by application of the CVT synthesis technique to Mo–V and Mo–W mixed oxide systems which will be treated in a subsequent study.

Acknowledgements

U. Wild, D. Frickel, and E. Gaigneaux are gratefully acknowledged for their help with the UPS/ISS/XPS experiments. This work has been supported by Deutsche Forschungsgemeinschaft, SFB 546, and by Fonds der Chemischen Industrie. Further, one of the authors (R.T.-S.) thanks the Alexander-von-Humboldt Foundation for a Roman-Herzog fellowship.

References

[1] E.R. Braithwaite, J. Haber (Eds.), Molybdenum: an outline of its chemistry and uses, Studies in Inorganic Chemistry, vol. 19, Elsevier, Amsterdam, 1994.
[2] H.K. Kung, Transition metal oxides: surface chemistry and catalysis, in: B. Delmon, J.T. Yates (Eds.), Studies in Surface Science and Catalysis, vol. 45, Elsevier, Amsterdam, 1989.
[3] R. Pearce, W.R. Patterson (Eds.), Catalysis and Chemical Processes, Wiley-Halsted, New York, 1981.
[4] J. Tichy, Appl. Catal. A 157 (1999) 363.
[5] T. Ilkenhans, B. Herzog, T. Braun, R. Schlögl, J. Catal. 153 (1995) 275.
[6] R. Böhling, A. Drochner, M. Fehlings, D. Knig, H. Vogel, Chem. Ing. Tech. 71 (1999) 3199.
[7] H. Böhnke, J.C. Petzold, B. Stein, C. Weimer, J.W. Gaube, DGMK Tagungsbericht 9803, in: G. Emig, C. Kohlpaintner, B. Lücke (Eds.), Proc. DGMK Conf.: Selective Oxidations in Petrochemistry, Hamburg, DGMK, Hamburg, 1998, p. 65.

[8] T. Ekström, M. Nygren, Acta Chem. Scand. 26 (1972) 1827.
[9] L. Kihlborg, Acta Chem. Scand. 23 (1969) 1834.
[10] K. Brückman, R. Grabowski, J. Haber, A. Mazurkiewicz, J. Slocynski, T. Wiltowski, J. Catal. 104 (1987) 71.
[11] N. Yamazoe, L. Kihlborg, Acta Cryst. B 31 (1975) 1666.
[12] J. Tichy, J. Kusta, J. Venkl, Coll. Czechos. Chem. Commun. 39 (1974) 1797.
[13] V.C. Malshe, S.B. Chandalia, J. Appl. Chem. Biotechnol. 27 (1977) 575.
[14] R.K. Grasselli, J.D. Burrington, Adv. Catal. 30 (1981) 133.
[15] J. Tichy, J. Kusta, J. Machek, Coll. Czechos. Chem. Commun. (1982) 698.
[16] M. Ai, Appl. Catal. 27 (1986) 167.
[17] L.M. Plyasova, L.P. Solovéva, G.N. Kryukova, T.V. Andrushkevich, Kinet. Catal. 31 (1990) 1253.
[18] T.V. Andrushkevich, V.M. Bondareva, G.Y. Popova, L.M. Plyasova, Stud. Surf. Sci. Catal. 72 (1992) 91.
[19] T.V. Andrushkevich, Catal. Rev. Sci. Eng. 35 (1993) 213.
[20] S. Breiter, M. Estenfelder, H.-G. Lintz, A. Tenten, H. Hibst, Appl. Catal. A 134 (1996) 81.
[21] A. Magneli, Nature 115 (1950) 356.
[22] A. Magneli, B. Blomberg, L. Kihlborg, G. Sundkvist, Acta Chem. Scand. 9 (1955) 1382.
[23] L. Kihlborg, Ark. Kemi 21 (1963) 443.
[24] G. Hägg, A. Magneli, Ark. Kemi 19 (1944) 1.
[25] A. Magneli, G. Anderson, B. Blomberg, L. Kihlborg, Anal. Chem. 24 (1952) 1998.
[26] A. Magneli, Acta Cryst. 6 (1953) 495.
[27] T. Ekström, E. Salje, R.J.D. Tilley, J. Solid, State Chem. 40 (1981) 75.
[28] E. Salje, R. Gehlig, K. Viswanathan, J. Solid, State Chem. 25 (1978) 239.
[29] H. Werner, O. Timpe, D. Herein, Y. Uchida, N. Pfänder, U. Wild, R. Schlögl, H. Hibst, Catal. Lett. 44 (1997) 153.
[30] G. Mestl, C. Linsmeier, R. Gottschall, M. Dieterle, J. Find, D. Herein, J. Jäger, Y. Uchida, R. Schlögl, J. Mol. Catal. A 162 (2000) 455.
[31] M. Dieterle, G. Mestl, J. Jäger, Y. Uchida, H. Hibst, R. Schlögl, J. Mol. Catal. A: Gen., in press.
[32] P. Gai-Boyes, Catal. Rev. Sci. Eng. 34 (1992) 1.
[33] J. Haber, E. Lalik, Catal. Today 33 (1997) 119.
[34] A. Bielanski, J. Haber, Oxygen in Catalysis, Marcel Dekker, New York, 1991.
[35] J. Haber, B. Grzybowska, J. Catal. 28 (1973) 489.
[36] B. Grzybowska, J. Haber, J. Janas, J. Catal. 49 (1977) 150.
[37] J. Haber, Pure Appl. Catal. 50 (1978) 923.
[38] F. Weiss, J. Marion, J. Metzger, J.M. Cognion, Kinet. Katal. 14 (1973) 45.
[39] J.C. Volta, J.L. Portefaix, Appl. Catal. 18 (1985) 1.
[40] J.C. Volta, J.M. Tatibouet, J. Catal. 93 (1985) 467.
[41] M. Abon, J. Massardier, B. Mingot, J.C. Volta, N. Floquet, O. Bertrand, J. Catal. 134 (1992) 542.
[42] M.A. Banares, J.L.G. Fierro, J.B. Moffat, J. Catal. 142 (1993) 406.
[43] A. Parmaliana, F. Arena, J. Catal. 167 (1997) 75.
[44] A. Bielanski, M. Najbar, Appl. Catal. 157 (1997) 223.
[45] J.M. Tatibouet, J.E. Germain, J. Catal. 72 (1981) 375.
[46] A. Baiker, D. Gasser, Z. Phys. Chem. 149 (1986) 119.
[47] B. Grzybowska-Swierkosz, Appl. Catal. A: Gen. 157 (1997) 409.
[48] F. Trifiro, I. Pasquon, J. Catal. 12 (1968) 412.
[49] J. Guidot, J.E. Germain, React. Kinet. Katal. Lett. 15 (1980) 389.
[50] T. Wadayama, T. Saito, W. Suetaka, Appl. Surf. Sci. 20 (1984) 199.
[51] J.S. Chung, R. Miranda, C.O. Bennett, J. Catal. 114 (1988) 398.
[52] E. Broclawik, J. Haber, J. Catal. 72 (1981) 379.
[53] E. Serwicka, Crit. Rev. Surf. Sci. 1 (1990) 27.
[54] A. Magneli, Ark. Kemi 1 (1950) 513.
[55] E. Serwicka, J. Solid State Chem. 51 (1984) 300.
[56] L. Kihlborg, Ark. Kemi 21 (1963) 357.
[57] A.B. Anderson, D.W. Ewing, Y. Kim, R.K. Grasselli, J.D. Durrington, J.F. Brazdil, J. Catal. 96 (1985) 222.
[58] A.R. Adams, T.J. Jennings, J. Catal. 3 (1964) 549.
[59] J. Haber, in G. Ertl, H. Knözinger, J. Weitkamp (Eds.), Handbook of Heterogeneous Catalysis, vol. 5, Wiley-VCh, Weinheim, 1997, p. 2253ff.
[60] M. Niwa, M. Mizutani, M. Takahashi, Y. Murakami, J. Catal. 70 (1981) 14.
[61] K.T. Queeney, C.M. Friend, J. Phys. Chem. B 104 (2000) 409.
[62] L.E. Firment, A. Ferretti, Surf. Sci. 129 (1983) 155.
[63] S.C. Street, D.W. Goodman, J. Vac. Sci. Technol. A 15 (1997) 1717.
[64] M. Chen, U.V. Waghmare, C.M. Friend, E. Kaxiras, J. Chem. Phys. 109 (1998) 6854.
[65] A. Papakondylis, P. Sautet, J. Phys. Chem. 100 (1996) 10681.
[66] M.A. Py, P.E. Schmid, J.T. Vallin, Il Nouvo Cimento B 38 (1977) 271.
[67] M.A. Py, K.A. Maschke, Physica B 105 (1981) 376.
[68] A. Michalak, K. Hermann, M. Witko, Surf. Sci. 366 (1996) 323.
[69] K. Hermann, A. Michalak, M. Witko, Catal. Today 32 (1996) 321.
[70] K. Hermann, M. Witko, A. Michalak, ACS – Symposium on Advanced and Applications of Computational Chemical Modeling to Heterogeneous Catalysis, ACS Preprint, San Francisco, vol. 42, 1997, p. 106.
[71] K. Hermann, M. Witko, A. Michalak, Catal. Today 50 (1999) 567.
[72] R. Tokarz-Sobieraj, K. Hermann, M. Witko, to be published.
[73] J.K. Labanowski, J.W. Andzelm (Eds.), Density Functional Methods in Chemistry, Springer, New York, 1991.
[74] N. Godbout, D.R. Salahub, J. Andzelm, E. Wimmer, Can. J. Phys. 70 (1992) 560.
[75] J. Andzelm, E. Radzio, D.R. Salahub, J. Chem. Phys. 83 (1985) 4573.
[76] J.P. Perdew, K. Burke, M. Ernzerhof, Phys. Rev. B 59 (1999) 7413.

[77] B. Hammer, L.B. Hansen, J.K. Norskov, Phys. Rev. B 59 (1999) 7413.
[78] R.S. Mulliken, J. Chem. Phys. 23 (1955) 1833.
[79] R.S. Mulliken, J. Chem. Phys. 23 (1955) 1841.
[80] R.S. Mulliken, J. Chem. Phys. 23 (1955) 2388.
[81] R.S. Mulliken, J. Chem. Phys. 23 (1955) 2343.
[82] I. Mayer, Chem. Phys. Lett. 97 (1983) 270.
[83] I. Mayer, J. Mol. Struct. (Theochem) 149 (1983) 270.
[84] A.A. Bolzan, B.J. Kennedy, C.J. Howard, Aust. J. Chem. 48 (1995) 1473.
[85] K. Hermann, M. Witko, R. Druzinic, A. Chakrabarti, B. Tepper, M. Elsner, A. Gorschlüter, H. Kuhlenbeck, H.J. Freund, J. Electron, Spectrosc. Rel. Phenom. 98/99 (1999) 245.
[86] M. Hybertsen, S.G. Louie, Comments Condes. Matter Phys. 13 (1987) 5.
[87] K. Hermann, M. Witko, Druzinic, R. Tokarz, Topics Catal. 11/12 (2000) 67.
[88] G. Mestl, P. Ruiz, B. Delmon, H. Knözinger, J. Phys. Chem. 98 (1994) 11269.
[89] K. Hermann, M. Witko in: D.P. Woodruff (Ed.), The chemical physics of solid surfaces, vol. 9, Oxide Surface, Elsevier Science, Amsterdam, 2001.
[90] K. Hermann, M. Witko, R. Druzinic, Faraday Discuss. 114 (1999) 53.
[91] K. Hermann, M. Witko, R. Druzinic, R. Tokarz, Appl. Phys. A 72 (2000) 429.
[92] M. Dieterle, G. Mestl, to be published.